Article

Not peer-reviewed version

Ice Crystal Sedimentation Errors Arising from Weighted Fall Velocity in Three-Moment Bulk Cloud Microphysics Scheme

Xiangjun Shi * , Gongqi Jin , Jiarui Ma

Posted Date: 12 February 2026

doi: 10.20944/preprints202602.0956.v1

Keywords: weighted fall velocity; errors mechanisms; bulk cloud scheme

Article

Ice Crystal Sedimentation Errors Arising from Weighted Fall Velocity in Three-Moment Bulk Cloud Microphysics Scheme

Xiangjun Shi [1,2,*], Gongqi Jin [1] and Jiarui Ma [1]

[1] School of Atmospheric Sciences, Nanjing University of Information Science and Technology, Nanjing 210044, China.

[2] Earth System Modeling Center, Nanjing University of Information Science and Technology, Nanjing 210044, China.

* Correspondence: shixj@nuist.edu.cn

Abstract

This study investigates ice crystal sedimentation calculation errors arising from three-moment bulk cloud scheme. Both offline tests and one-dimensional cloud model simulations indicate that sedimentation calculation errors are most pronounced at both the cloud bottom and cloud top. At the cloud bottom, the error stems from how the bulk method treats ice crystal sedimentation. Specifically, the method uses three weighted fall velocities (corresponding to the three moments) to represent instantaneous fluxes through a fixed altitude, which inherently assumes that falling ice crystals can only affect the adjacent model layer below. This assumption artificially constrains the falling distance of larger ice crystals. At the cloud top, the differences among these three weighted fall velocities can give rise to physical inconsistencies. This issue is handled by artificial adjustment, which leads to a spurious narrow size distribution shape of ice crystals, especially under model configurations with coarse temporal resolution (large dT) and fine vertical resolution (small dH). If only the sedimentation process is considered, the above calculation errors can be effectively minimized by lowering the dT/dH ratio.

Keywords: weighted fall velocity; errors mechanisms; bulk cloud scheme

---

1. Introduction

Cirrus clouds (including thin cirrus) cover about 30% of the Earth's surface and play an indispensable role in weather and climate systems [1–26]. Unfortunately, owing to the complexity of ice-phase cloud microphysical processes [27–46], ice-phase cloud microphysics schemes remain a longstanding weakness of atmospheric models [47–66]. Considering computational cost, cloud microphysics schemes incorporated in atmospheric models do not resolve individual cloud particles (e.g., an ice crystal), but only characterize their macro-statistical properties. Two distinct approaches have emerged since their inception: bulk microphysics parameterization and spectral bin microphysics [67–70]. The bin approach explicitly represents cloud particle size distributions using tens to hundreds of bins, but its computational cost is prohibitively high due to extensive interactions between different bins [71–76]. By contrast, the bulk approach characterizes the particle size distributions via a semi-empirical distribution function; it boasts high computational efficiency and has thus been widely adopted in atmospheric models, especially for long-term climate simulations [77–90].

In the bulk schemes developed in this century, the particle size distribution is mostly described by the gamma distribution function with three parameters, namely, the intercept parameter (N_0), the slope parameter (λ), and the spectral shape parameter (μ) [91–93]. The currently widely used two-moment bulk schemes only predict the variations of N_0 and λ, while μ is assigned a fixed value or calculated via empirical formulas [52,94–96]. Unlike two-moment schemes, three-moment schemes are capable of predicting the variation of μ, enabling more realistic simulations of cloud microphysical processes and their impacts on weather and climate. Therefore, three-moment schemes have garnered growing attention in recent years [97–103].

The sedimentation process of ice crystals plays an important role in cirrus cloud evolution [104–108]. In two-moment bulk schemes, the number and mass of ice crystals within each model layer are predicted separately using number-weighted and mass-weighted fall velocities. The discrepancy between these two weighted velocities can, to a certain extent, represent the cloud particle size-sorting effect induced by sedimentation (i.e., small ice crystals remain aloft, whereas large ones settle downward). By incorporating an additional weighted fall velocity, three-moment schemes can further quantify the impact of sedimentation process on the shape of ice crystal size distribution (i.e., μ), thus enabling a more accurate representation of ice crystal sedimentation process [109–112]. Similar to the inevitable numerical computational errors in the dynamical cores of atmospheric models, such systematic errors also arise when bulk cloud schemes simulate ice crystal sedimentation process via weighted fall velocities [113]. However, few studies have conducted in-depth analyses of or explored the underlying mechanisms behind such errors in three-moment bulk schemes. This study aims to fill this research gap.

In this study, to investigate the numerical computational errors arising from weighted fall velocities in bulk schemes, we developed an idealized one-dimensional (1D) cirrus cloud model that includes only the sedimentation process. Besides the three-moment bulk scheme, the bin scheme was also utilized. Simulations from the bin scheme usually serve as a reference for evaluating the bulk scheme [68,114]. This paper is organized as follows: Section 2 introduces the 1D cloud model and describes the experimental setup. Section 3 analyses the calculation errors arising from the bulk scheme. Section 4 discusses the potential impacts of such errors and their relationship with ice crystal size distribution. Finally, Section 5 presents the conclusions. In addition, the Abbreviation section provides a comprehensive list of all symbols used in this paper.

2. Model and Experiments

2.1. Gamma Size Distribution and Three-Moment Bulk Scheme

To better understand the error mechanism, it is necessary to first clarify how the three-moment bulk scheme represents the ice crystal size distribution. Consistent with commonly adopted bulk schemes, number (N), mass (Q), and radar reflectivity factor (Z) are the three prognostic variables of the three-moment bulk scheme here, with each representing the corresponding content per unit air mass. Ice crystals are assumed to be spherical and to follow a gamma size distribution:

$$N'(D) = N_0 D^{\mu} e^{-\lambda D} \quad (1)$$

where $N'(D)$ is the number density (i.e., $\delta N/\delta D$) of the ice crystals with diameter D [97]. The k^{th} moment of this size distribution (M_k) can be expressed in the following form:

$$M_k = \int_0^{\infty} N_0 D^{\mu+k} e^{-\lambda D}\, dD = N_0 \Gamma(k+\mu+1) / \lambda_i^{(k+\mu+1)} \quad (2)$$

It can be readily concluded that $N = M_0$, $Q = cM_3$, and $Z = M_6$ where $c = \rho_i \pi/6$, ρ_i is the mass density of ice crystals [101]. Below is a description of how to derive the properties of ice crystal size distribution (i.e., N_0, λ, and μ) from these three moments (i.e., N, Q, and Z). Based on the recursive property of gamma function (i.e., $\Gamma(x+1) = x\Gamma(x)$), the following equation can be obtained:

$$G(\mu) = \frac{(\mu+4)(\mu+5)(\mu+6)}{(\mu+1)(\mu+2)(\mu+3)} = \frac{M_0 M_6}{{M_3}^2} = c^2 \frac{NZ}{Q^2} \quad (3)$$

Since the μ is defined as a non-negative value in the bulk scheme [48,112], G(μ) is a monotonic function of μ (Equation 3). In other words, μ can be derived from G(μ) [101]. Given that μ is known, λ and N_0 can be calculated via the following equations [94]:

Preprints.org (www.preprints.org) | NOT PEER-REVIEWED | Posted: 12 February 2026 doi:10.20944/preprints202602.0956.v1

$$\lambda = [\frac{cN}{Q}\frac{\Gamma(4+\mu)}{\Gamma(1+\mu)}]^{1/3} \tag{4}$$

$$N_0 = \frac{N\lambda^{(\mu+1)}}{\Gamma(1+\mu)} \tag{5}$$

Figure 1 shows the normalized size distribution shapes (i.e., the relative contributions of each bin) for different μ values and the variation of function G(μ) with μ. At μ= 0, the size distribution exhibits the broadest shape, with the corresponding G attaining a maximum value of 20 (Equation 3). With the increase in μ, the size distribution shape becomes narrower, while G exhibits a rapid decrease. At μ= 10, the value of G has dropped to 1.96. When μ> 10, G decreases very slowly. Meanwhile, it is difficult to accurately derive μ from G. This is the reason why the upper limit of μ is usually set to 20 in the three-moment scheme (e.g., [99,111]). In this study, the upper limit of μ is set to 40 in order to capture a wider range of size distribution shapes, particularly narrower ones. Correspondingly, the lower limit of G is 1.23. At the model initialization, we pre-calculate 65 pairs of μ and G values as reference points, which are shown by the solid dots on the curve in the right panel of Figure 1. The process for deriving μ from G is as follows: first, determine which two reference points the given G value lies between; then obtain the corresponding μ value via linear interpolation.

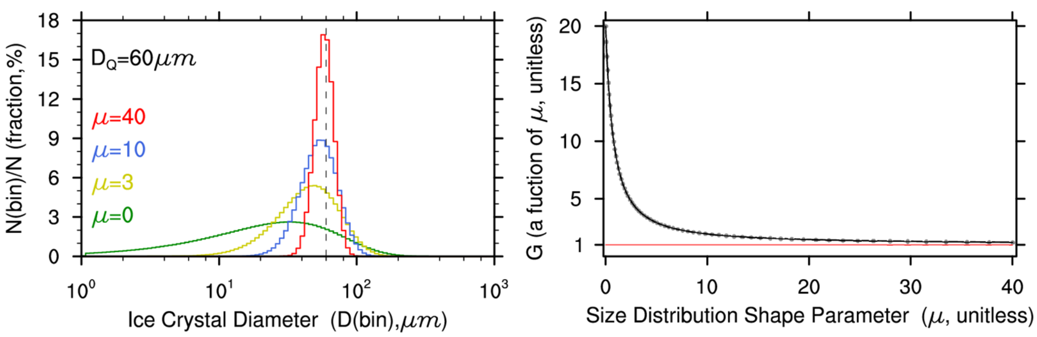

Figure 1. Ice crystal size distribution shapes corresponding to different μ values under the same mass-weighted diameter (D_Q= 60 μm) (left panel) and the variation of function G(μ) with μ (right panel). The size distribution plot shows the relative number contributions from each bin (i.e, the ratio of the number within each size bin *N*(bin) to the total number *N*). All bins have the same width, which is defined based on the logarithm of ice crystal diameters. A total of 100 bins were used here. The plot of G(μ) is constructed from 65 pairs of μ values (0~40) and corresponding G values (20~1.23).

It is noteworthy that the shape of normalized size distribution is determined solely by μ, and is independent of the mass-weighted diameter of ice crystals (D_Q). In Figure 1, the D_Q is set to 60 μm. Increasing or decreasing D_Q will shift the size distribution shape to the right or left, respectively (not shown). In this study, 100 size bins are defined over the diameter interval of 1~1000 μm. For an intuitive illustration of the gamma size distributions determined by the three moments (i.e., *N*, *Q*, and *Z*), the ice crystal concentration per size bin can be derived from gamma distribution parameters (i.e., N_0, λ, and μ) with Equation 1 and visualized in plots analogous to the left panel of Figure 1. In other words, this is a mapping from bulk properties (*N*, *Q*, and *Z*) to bin properties (the *N* in each individual size bin). To better reflect correlations between physical quantities via their naming convention, the suffix '(bin)' is used to indicate the value of a physical quantity in each size bin. For example, *N*(bin) refers to the number in each individual size bin, with the *N* being the summation of *N*(bin) over all bins. Furthermore, if 'bin' in the parentheses refers to a certain serial number, it represents the physical quantity within that serial-numbered bin. For example, *N*(5) refers to the ice crystal number in the 5th bin.

Preprints.org (www.preprints.org) | NOT PEER-REVIEWED | Posted: 12 February 2026 doi:10.20944/preprints202602.0956.v1

2.2. Ice Crystal Fall Velocities in Bin and Bulk Schemes

Observational studies have shown that the ice crystal fall velocity (*V*) typically follows a power-law relationship with diameter *D* and is also influenced by air density [115,116]. Following the cloud scheme developed by Gettelman et al. (2015) [86], *V* is calculated via this empirical formula:

$$V(D) = (\rho_{a850}/\rho_a)^{0.35} a D^b \tag{6}$$

where ρ_{a850} is the reference air density at 850 hPa and 273.15 K, ρ_a is the ambient air density, a and b are empirical coefficients (see Abbreviations). Here,$(\rho_{a850}/\rho_a)^{0.35}$ represents the impact of ambient air density. In this study, to avoid the influence of varying ambient air density on V, the ambient atmospheric pressure and temperature are fixed at 500 hPa and 230 K, respectively, across all altitudes. In other words, *V* depends exclusively on *D*. Consequently, within the bin scheme (i.e., 100 bins covering the *D* range of 1~1000 μm), *V*(bin) are held constant. To facilitate a more rigorous comparison with the results of the bin scheme, the number-weighted, mass-weighted, and radar reflectivity factor-weighted fall velocities (V_N, V_Q, and V_Z) employed in the bulk scheme are calculated from *V*(bin), with the corresponding formula presented below:

$$V_N = \sum_{bin=1}^{100} V(bin)N(bin) \Big/ \sum_{bin=1}^{100} N(bin) \tag{7}$$

$$V_Q = \sum_{bin=1}^{100} V(bin)N(bin)D(bin)^3 \Big/ \sum_{bin=1}^{100} N(bin)D(bin)^3 \tag{8}$$

$$V_Z = \sum_{bin=1}^{100} V(bin)N(bin)D(bin)^6 \Big/ \sum_{bin=1}^{100} N(bin)D(bin)^6 \tag{9}$$

The *V*(bin) are shown in Figure 2. At the 17th size bin, *D*(17)= 3.02 μm and corresponding *V*(17)= 0.25 cm s^{-1}. At this fall velocity, the ice crystals descend only 4.5 meters within half an hour. At the 34th size bin, *D*(34)= 9.77 μm and corresponding *V*(34)= 0.80 cm s^{-1}. At this fall velocity, the ice crystals descend 14.4 meters within half an hour. When *D*> 10 μm, the trend that V increases with rising ln*D* becomes obvious. Figure 2 also shows normalized size distributions (in terms of the number, mass, and radar reflectivity factor, respectively) and weighted fall velocities (i.e., V_N, V_Q, and V_Z) under the scenario of D_Q= 60 μm and μ= 2. The V_N, V_Q, and V_Z are 3.65 cm s^{-1}, 7.31 cm s^{-1}, and 11.01 cm s^{-1}, respectively. Using the fall velocity formula (Equation 6), it can be calculated that when the fall velocity is equal to V_N (i.e., 3.65 cm s^{-1}), the corresponding equivalent *D* is 45.95 μm. In normalized number distribution, *D*= 45.95 μm is close to the median value, and the contribution of its corresponding bin is the highest. The equivalent *D* for V_Q increases to 92.13 μm because the proportion of large-size bins rises significantly after multiplication by mass (i.e., *D*(bin)^3). Correspondingly, in the normalized mass distribution, *D*= 92.13 μm lies near the median value, and the contribution of its corresponding bin is the highest. Furthermore, as compared to the normalized number distribution, the distribution shape becomes narrow and the peak bin shifting to larger *D*. The equivalent *D* associated with V_Z reaches an even higher value of 138.74 μm. This value also lies near the median in the corresponding normalized size distribution, and its corresponding bin exhibits the maximum contribution. From the perspective of ice crystal instantaneous fluxes through a fixed altitude level, the V_N, V_Q, and V_Z reasonably characterize, respectively, the variation trends of *N*, *Q*, and *Z* in the current model layer.

doi:10.20944/preprints202602.0956.v1

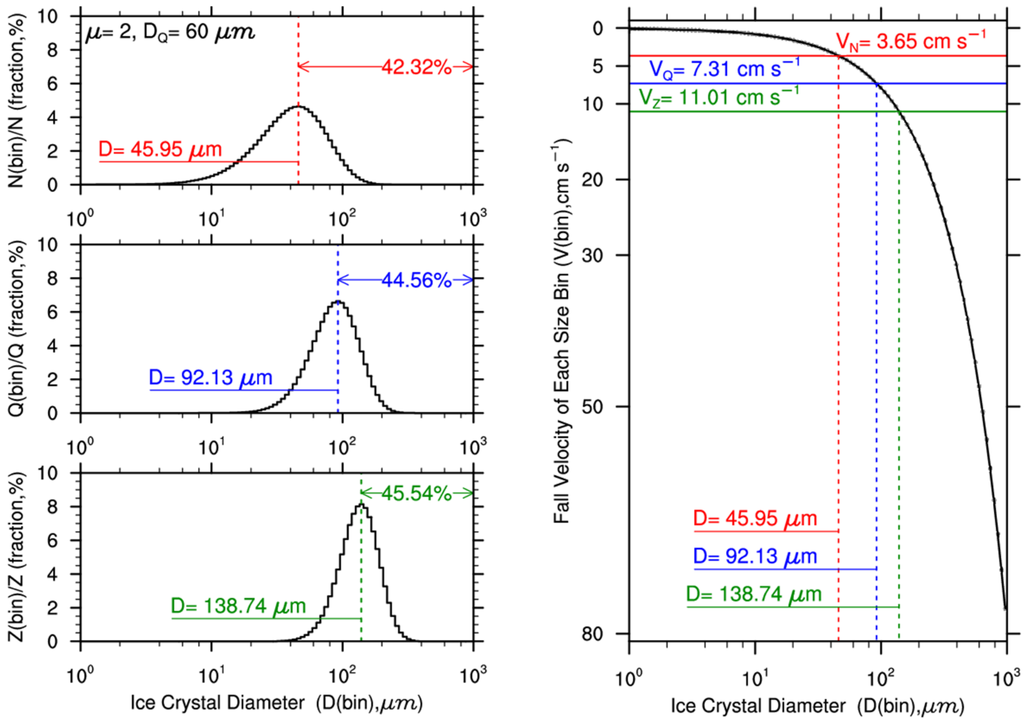

Figure 2. The relative number, mass, and radar reflectivity factor contributions from each size bin (*N*(bin)/*N*, *Q*(bin)/*Q*, and *Z*(bin)/*Z*, left panel) and fall velocities of each size bin and number, mass, and radar reflectivity factor-weighted values (*V*(bin), V_N, V_Q, and V_Z, right panel). Here, the ice crystal size distribution scenario is mass-weighted diameter D_Q= 60 μm and shape parameter μ= 2.

2.3. Idealized 1D Cirrus Cloud Model

The total simulated height of the idealized 1D model is a preset configuration parameter, with a default value of 4 km. The height of each model layer is defined using relative altitude, with Height= 0 km denoting the model top. The thickness of each model layer (dH) is uniform, with a tuneable value ranging from 10 to 200 m (the value should be divisible by the total simulated height). The tuneable time step (dT) for model simulation ranges from 10 to 1800 s. The sedimentation process is treated using two approaches: the bin scheme and the bulk scheme. The calculation methods of these two schemes are derived from the relevant descriptions in previous studies [94,97,109,111,113,117], with certain detailed treatments referenced from the accessible model source code corresponding to these studies.

Taking the analysis of ice crystal sedimentation within a specific layer as an illustrative example, this paragraph elaborates on the calculating method with the bin scheme. The model framework parameters dH and dT are configured to 200 m and 1800 s, respectively. At the 34th size bin, *D*(34)= 9.77 μm and *V*(34)= 0.80 cm s^{-1}. After one model time step, the sedimentation distance of ice crystals within this size bin is calculated as H_{sed}= *V*(34)×dT= 14.40 m. The fraction of ice crystals (in terms of number) within this size bin that fall into the adjacent lower model layer is given by H_{sed}/dH= 7.2%. Correspondingly, 92.8% remains in the current layer. At the 73rd size bin, *D*(73)= 149.62 μm and *V*(73)= 11.87 cm s^{-1}. After one model time step, the sedimentation distance of these ice crystals is H_{sed}= *V*(73)×dT= 213.66 m. For this size bin, all ice crystals sediment out of the current layer, the fraction that falls into the adjacent layer is 2− H_{sed}/dH= 93.17%, and the fraction that falls into the second layer is H_{sed}/dH−1= 6.83%. Based on the aforementioned method, the sedimentation destination of ice crystals in each size bin within every layer can be quantitatively determined, thereby enabling the numerical calculation of ice crystal sedimentation process.

This paragraph illustrates how the bulk scheme calculates the sedimentation process based on the size distribution scenario of D_Q= 60 μm and μ= 2 with V_N= 3.65 cm s−1, V_Q= 7.31 cm s^{-1}, and V_Z=11.01 cm s^{-1} (Figure 2). Because these weighted fall velocities (V_N, V_Q, and V_Z) represent crystal

Preprints.org (www.preprints.org) | NOT PEER-REVIEWED | Posted: 12 February 2026 doi:10.20944/preprints202602.0956.v1

instantaneous fluxes (*N*, *Q*, and *Z*) through a fixed altitude level, it is reasonable to assume that the falling ice crystals can only affect the adjacent model layer below (i.e., restriction on falling distance). After one model time step, the fractions of ice crystal *N*, *Q*, and *Z* that are lost from the current layer are given as V_N×dT/dH, V_Q×dT/dH, and V_Z×dT/dH, respectively. For the configuration with dH=200 m and dT=900 s, V_N×dT/dH= 16.43%, V_Q×dT/dH= 32.90%, and V_Z×dT/dH= 49.55%. By number, 16.43% of ice crystals fall into the adjacent lower layer. This 16.43% of ice crystals consists mainly of larger particles, accounting for 32.90% of total mass (i.e., *Q*) and 49.55% of total radar reflectivity factor (i.e., *Z*). Conversely, ice crystals remaining in the current layer consist mainly of smaller particles, representing 83.57% *N*, 67.10% *Q*, and 50.05% *Z*. For this case, the bulk scheme that calculates the evolution of ice crystal properties (*N*, *Q*, and *Z*) via weighted fall velocities (V_N, V_Q, and V_Z) seems reasonable. However, inconsistencies arise when the model is configured with dH=200 m and dT=1800 s. After one time step, 32.85% *N*, 65.79% *Q*, and 99.09% *Z* fall into the adjacent lower layer. The *N*, *Q*, and *Z* of ice crystals remaining in the current layer correspond to 67.15%, 34.21%, and 0.91%, respectively. From Equation 3, we can easily derive that G(μ) is 5.22% of its initial value (i.e., G(μ)= 5.90 at μ= 2), which gives a resultant value of G(μ)= 0.31. This value is out of the pre-defined G range (Figure 1). Bulk cloud schemes typically handle such issues by artificially adjusting the value to preset range [68]. In the above case, G is adjusted to its lower limit, which corresponds to μ= 40. Meanwhile, *Z* is also adjusted based on Equation 3. Furthermore, there is another inconsistency issue in which V_Q×dT/dH falls into the second lower layer, whereas V_N×dT/dH does not, such as the configuration of dH=100 m and dT=1800 s. This issue is resolved by substepping the time step [94]. By reducing the model time step (i.e., sub-step), it is ensured that the weighted fall velocities (V_N, V_Q, and V_Z) can only affect the adjacent model layer below within one model time sub-step. Here, one time step (dT=1800 s) will be divided into two sub-steps (dT=900 s). After the 1st sub-step, 32.85% *N*, 65.79% *Q*, and 99.09% *Z* fall into the adjacent lower layer (same as the configuration of dH=200 m and dT=1800 s). Correspondingly, 67.15% *N*, 34.21% *Q*, and 0.91% *Z* remains in the current layer. During the 2nd sub-step, sedimentation of ice crystals in the current layer is still governed by the previously determined weighted fall velocities, which are used to calculate the proportion falling into the layer below. Subsequently, the final ice crystals properties in the current layer can be obtained (i.e., 45.09% *N*, 11.70% *Q*, and, 0.01% *Z*). The ice crystals that fall out of this layer constitute the source term for adjacent layer below. Overall, the constraint that ice crystals can only fall into the adjacent layer within one model time step (i.e., all sub-steps) is also enforced here.

2.4. Experimental Design

All model experiments in this study adopt an identical initial setting. At the initial time, ice crystals exist only in the model layers between −0.4 km and −0.8 km. Furthermore, the ice crystal properties are uniform across all cloud-containing model layers. D_Q= 60 μm, μ= 2 and *N*= 300 g^{-1}. From these three physical quantities, we can further diagnose *Q*, *Z*, and *N*(bin). It is noteworthy that *N*, *Q*, and *Z* in cloud schemes represent the content per unit mass of air (e.g., g^{-1}), which could avoid variations induced by cloud parcel expansion. However, the *N*, *Q*, and *Z* output by the model are converted to the commonly used content per unit volume of air (e.g., L^{-1}).

From the above introduction to the bulk scheme, it is clear that the simulation results are closely related to the setting of model spatiotemporal resolution (i.e., dH and dT). Consistent with the three types of model configurations mentioned in the above subsect, three experiments with different model configurations are conducted herein. For clarity, all experiments are named based on the model resolution. The dH200dT900 experiment (i.e., with the configuration of dH=200 m and dT=900 s) could effectively mitigate the occurrence of inconsistency issues. In the dH200dT1800 experiment, the operation of shifting G into the preset range will be invoked frequently. The dH100dT1800 experiment will trigger sub-step treatment. For each configuration, a pair of experiments was designed: one using the bulk scheme (hereafter BULK), and a corresponding experiment using the bin scheme (hereafter BIN). Each experiment is run for 120 minutes, with simulation results output at the initial time, the 30th minute, and the 120th minute.

 doi:10.20944/preprints202602.0956.v1

3. Results

3.1. Off-Line Tests

To better understand the 1D cloud model simulation bias from experiments with bulk scheme, we firstly illustrated three off-line tests. In terms of spatiotemporal resolution, these three off-line tests correspond to the three aforementioned model experiments. Additionally, at the initial time, D_Q= 60 μm and μ= 2 are consistent with the initial settings of model experiments. The only difference is that ice crystals exist exclusively in the top layer of the model (only one model layer). The specific data of ice crystals vertical distribution 30 minutes after the onset of sedimentation is summarized in Table 1.

Under the configuration of dH= 200 m and dT= 900 s, the 30th minute state is derived after 2 time steps. The calculation results of the bin scheme show that 70.8% of the ice crystals (i.e., 70.8% N) remain in the top layer, with their D_Q decreasing to 58 μm. As most of the larger ice crystals fall out while the smaller ones mostly remain suspended, the size distribution narrows and μ increases to 2.3. The ice crystals falling out from the top layer (−200m ~ 0) are mainly distributed in the second and third layers (−400m ~ −200m and −600m ~ −400m). The D_Q from second and third layers are 69.9 μm and 91.3 μm, respectively, which is consistent with the principle that larger ice crystals fall over longer distances. In the second layer, μ increases to 3.3 as sedimenting ice crystals are more concentrated at larger sizes; accordingly, μ in the third layer rises further to 4.0 as this effect intensifies. The above phenomena are consistent with the so-called size-sorting effect induced by sedimentation, namely that the ice crystal size distribution becomes more concentrated at each layer, with smaller crystals dominating at higher layer and larger ones prevailing at lower layer [68,109,111,113]. The results calculated by the bulk scheme are generally consistent with those from the bin scheme, indicating that the bulk scheme can well simulate the ice crystal sedimentation process under this scenario.

Table 1. The distribution of ice crystal properties after a 30-minute sedimentation.

Layers	BIN					BULK				
	N	Q	Z	D_Q	μ	N	Q	Z	D_Q	μ
dH= 200 m and dT= 900 s										
−200m ~ 0	70.8%	46.8%	28.2%	52.3μm	2.3	70.7%	46.8%	27.8%	52.3μm	2.3
−400m ~ −200m	25.6%	40.5%	44.6%	69.9μm	3.3	25.7%	40.4%	44.9%	69.8μm	3.2
−600m ~ −400m	3.6%	12.6%	27.1%	91.3μm	4.0	3.6%	12.6%	27.3%	91.2μm	3.9
dH= 200 m and dT= 1800 s										
−200m ~ 0	67.2%	36.3%	13.6%	48.8μm	3.3	67.2%	34.2%	0.9%	47.9μm	40
−400m ~ −200m	32.7%	61.7%	73.8%	74.2μm	3.8	32.8%	65.8%	99.1%	75.7μm	3.0
−600m ~ −400m	0.1%	2.0%	12.5%	181.2μm	37.4					
dH= 100 m and dT= 1800 s										
−100m ~ 0	39.5%	7.5%	0.7%	34.5μm	6.2	45.2%	11.7%	0.01%	38.3μm	40
−200m ~ −100m	55.6%	57.6%	25.9%	60.7μm	6.6	54.8%	88.3%	99.99%	70.31μm	3.2
−300m ~ −200m	4.8%	31.1%	51.3%	111.7μm	21.1					
−400m ~ −300m	0.1%	3.7%	19.2%	177.1μm	40					

*At the initial time, ice crystals exist only in the top layer. The N, Q, and Z all represent relative changes with respect to these values in the top layer at initial time. If the N is less than 0.1%, this layer will be excluded from presentation.

Under the configuration of dH= 200 m and dT= 1800 s, after 30 minutes of sedimentation, the bulk scheme shows that the μ of the ice crystals remaining in the top layer reaches its upper limit (40, see subsection 2.3). This value of μ is far from that of the bin scheme (3.3). Furthermore, with the bulk scheme, no ice crystals are present in the third layer. Actually, the ice crystals in the 73rd bin and all subsequent bins fall over a distance of 200 m, with a considerable proportion reaching the third layer (i.e., the bin scheme, see subsection 2.3). Correspondingly, the D_Q in this model layer is extremely large, reaching 181.2 μm. Since the ice crystals entering the third layer originate exclusively from the 73rd and subsequent bins (i.e., narrow size distribution), the corresponding μ is consequently increased to a remarkably high value (37.4, bin scheme). For the configuration discussed above (i.e., dH = 200 m and dT = 900 s), the bin scheme yields a μ value of 4.0 in the third layer. There exhibits an enormous discrepancy (37.4 vs 4.0) even the bin scheme is applied in both configurations. The reason is as follows: under dT= 900 s, the data presented in Table 1 are the results after two rounds of sedimentation calculations. Owing to the coarse spatial resolution (dH= 200 m), the numerical diffusion effect is pronounced [118,119], which allows ice crystals in smaller bin (< the 73rd) to fall into the third layer as well. As a result, the size distribution in the third layer becomes broader (i.e., smaller μ).

Under the configuration of dH= 100 m and dT= 1800 s, the discrepancy between the results of the bulk and bin schemes becomes even more pronounced. With the bin scheme, 31.1% and 3.7% of initial ice crystal mass fall into the third (−300m ~ −200m) and fourth (−400m ~ −300m) layers, respectively. Regarding radar reflectivity factor, a much higher proportion (51.3% and 19.2%) falls into the third and fourth layers. With the bulk scheme, although the substepping treatment is triggered, no ice crystals are present in the third and fourth layers because ice crystals can only fall into the adjacent layer. Furthermore, the μ at the top layer also reaches its upper limit (i.e., 40) with the bulk scheme, while the μ is 6.2 with the bin scheme. It is obvious that the bin scheme produces a wide range of simulated cloud-top μ under different model configurations. The configuration with higher dT/dH ratio enables more large ice crystal particles to fall out of the model layer. This process thereby narrows the size distribution of the remaining ice crystals and, consequently, increases the shape parameter μ.

In summary, when the configuration is prone to triggering sub-stepping or artificial adjustment with the bulk scheme (i.e., dT/dH is relatively high), simulations tend to exhibit the following biases: the μ at the cloud top layer might be spuriously high, and the falling distance of large ice crystals is inherently reduced to adjacent layer. In addition, the simulation results from the bin scheme show significant discrepancies under different configurations (i.e., different dT/dH).

3.2. Model Simulations

To facilitate the comparison of simulation results between the bin and bulk schemes, the 1D model outputs the N, Q, Z, D_Q, μ, and N(bin) in each model layer regardless of which scheme is employed. When using the bulk scheme, the D_Q, μ, and N(bin) are diagnosed from N, Q, and Z. When using the bin scheme, the N, Q, Z, D_Q, and μ are diagnosed from N(bin).

Figure 3 shows the evolution of ice crystals during sedimentation from the dH200dT900 experiments. In terms of bulk properties (i.e., N, Q, Z, D_Q, and μ; upper panel), the simulation results from the BULK and BIN experiments almost overlap with no significant differences observed. However, in terms of the bin properties (i.e., N(bin); lower panel), subtle yet distinguishable discrepancies between these two experiments can still be identified. For the small ice crystals with D< 3 μm, the falling distance is no more than 5 m within 30 minutes, and the loss of these small ice crystals in the current model layer does not exceed 5/200. This phenomenon is well demonstrated by the BIN experiment. However, the BULK experiment results show that the number of very small ice crystals (D< 3 μm) in initial cloud-containing layers (−0.8 km~ −0.4 km) exhibit a pronounced reduction. The reasons for this error are as follows. The bulk scheme characterizes the ice crystal particle size distribution based on three prognostic variables: N, Q, and Z. Here, the ice crystal particles are assumed to obey a gamma distribution. Unlike the initial state (gamma distribution), after some large ice crystal particles fall out, the ice crystal size distribution no longer strictly follows a gamma distribution. If a gamma function is still used to fit the size distribution of these remaining ice crystals, the gamma size distribution will become more concentrated toward the middle. The newly fitted gamma function can represent the reduction in large ice crystals while also generating an illusion of a decrease in small ice crystals. In contrast, the bin scheme is free from the constraint of gamma distribution assumption and thus does not have the above issue. To some extent, the difference between the BULK and BIN experiments arises from gamma fitting. The simulation results at the 120th minute show that the spurious reduction of small ice crystals in the initial cloud-containing layers becomes more pronounced. Overall, even if the bulk scheme can accurately capture the evolution of bulk properties (*N*, *Q*, and *Z*), errors induced by gamma fitting may still arise. However, such errors are confined to the bin properties (i.e., *N*(bin)). It should be noted that atmospheric models only adopt the bulk properties provided by the cloud scheme (i.e., *N*, *Q*, *Z*, N_0, λ, and μ), and thus errors in *N*(bin) exert no impact on the simulation results of host atmospheric models.

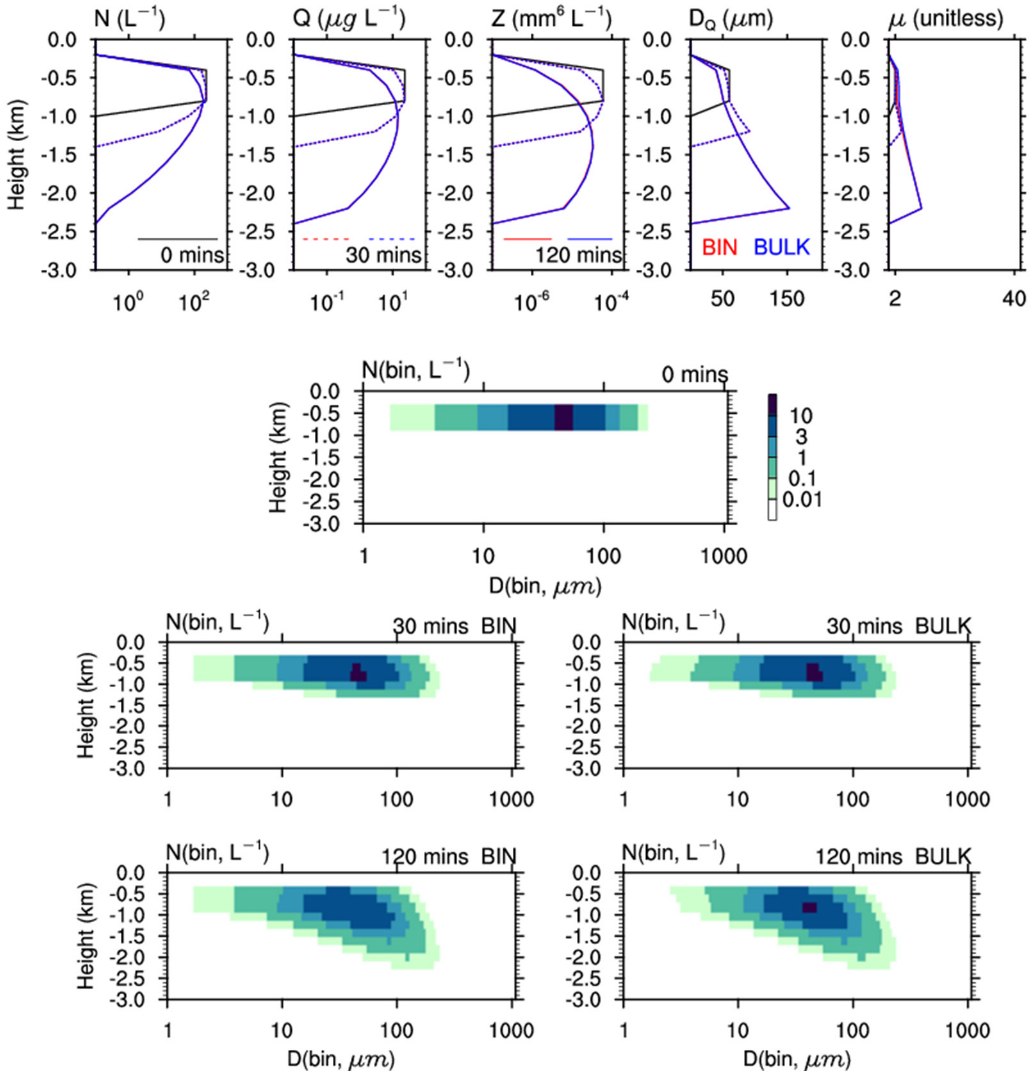

Figure 3. The evolution of ice crystals during sedimentation at the initial time, 30th minute, and 120th minute from the dH200dT900 experiments. The bulk and bin properties are shown in the upper and lower panels, respectively. In the upper panel, the labels of the specific bulk properties (*N*, *Q*, *Z*, D_Q, and μ) are shown above each subplot. The black solid lines indicate the initial state (i.e., the 0th minute). The colored dashed lines and solid lines indicate the states at the 30th and 120th minutes, respectively. In the lower panel, the bin properties (i.e., *N*(bin)) from the BIN and BULK experiments are presented in the left and right columns, respectively.

Figure 4 shows the evolution of ice crystals from the dH200dT1800 experiments. The bulk properties (i.e., *N*, *Q*, *Z*, D_Q, and μ) are analyzed (upper panel) firstly. Here, the simulation results of the BULK and BIN experiments exhibit a significant discrepancy. The ice crystal fall distance in the BIN experiment is obviously greater than that in the BULK experiment. At the 30th and 120th minutes, the D_Q at the cloud bottom layer from the BIN experiment is much larger than that from the BULK experiment. This is in agreement with the off-test (section 3.1). The μ at the cloud top layer from the

BULK experiment reaches the its upper limit (40) owing to artificial adjustment (subsection 2.3), whereas the BIN experiment is free of such error. This is also in agreement with the above off-test. The *N*(bin) plot (lower panel) more intuitively illustrates the difference between the BULK and BIN experiments. In the BIN experiment, ice crystals in the cloud top layer exhibit a broad size distribution, despite some large ice crystals falling out of this layer. However, the size distribution of ice crystals in the cloud top layer derived from the BULK experiment exhibits spurious concentration owing to the artificial adjustment on G(μ). At the 120th minute, the ice crystal size distribution from the BULK experiment is significantly narrower than that from the BIN experiment in most cloud-containing layers (excluding cloud top layer). This is mainly due to the gamma fitting implementation in the BULK experiment. In terms of ice crystal fall distance, ice crystals in the 73rd bin and subsequent bins (i.e., *D*> 144.54 μm) can fall into lower model layers in the BIN experiment, while the BULK experiment restricts the fall distance of these large ice crystals. This is the reason why the large ice crystals in the BIN experiment can fall below −1.6 km. Compared with the dH200dT900 experiments (dT/dH = 4.5 s m^{-1}, Figure 3), the dT/dH ratio in the dH200dT1800 experiments here (Figure 4) is doubled, reaching 9 s m^{-1}, and thus artificial adjustment (cloud top) and fall distance restriction (cloud bottom) are prone to occur, which induces biases in the simulation results (Figure 4).

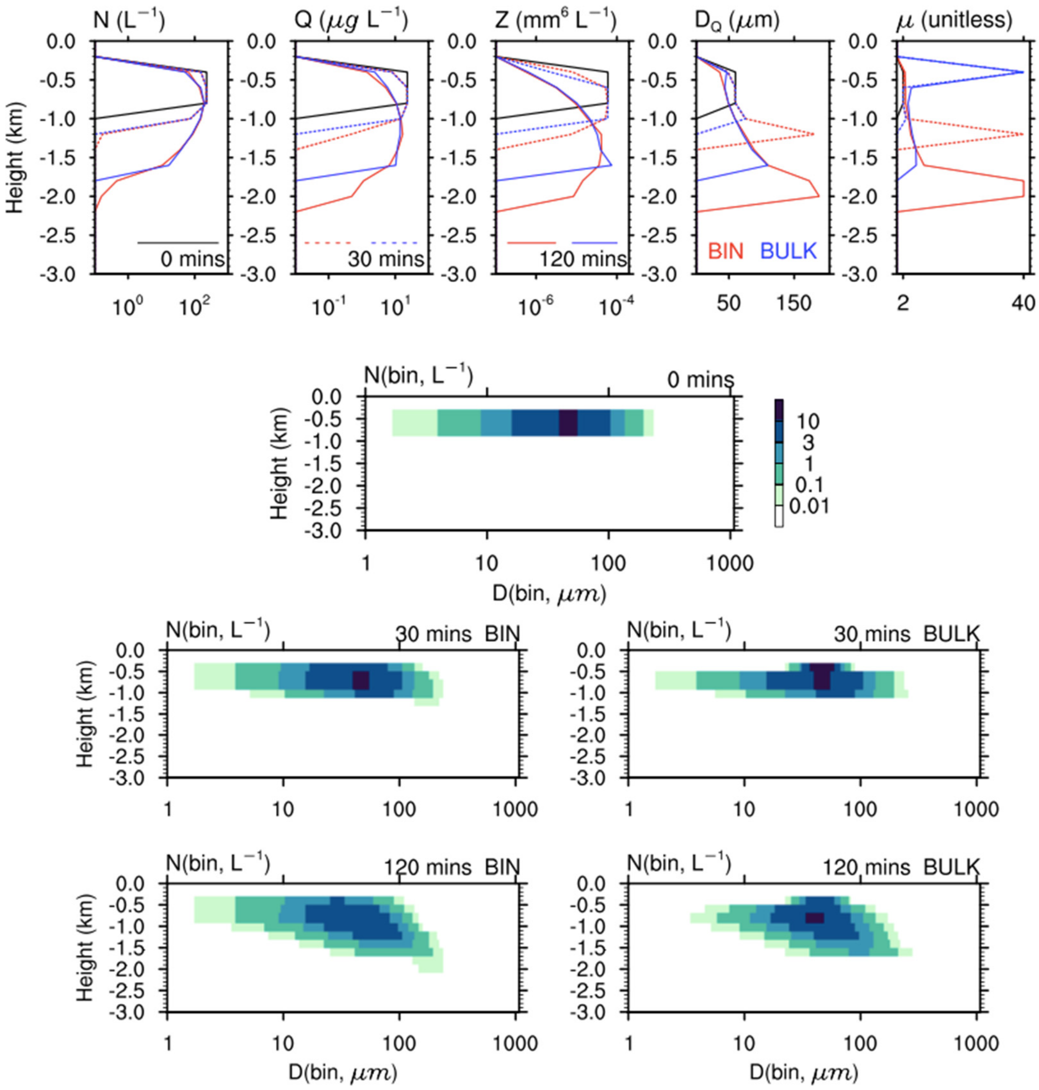

Figure 4. Similar as Figure 3, but for the dH200dT1800 experiments.

Figure 5 shows the simulation results from the dH100dT1800 experiments. Under this configuration with the bulk scheme, the sub-step treatment is invoked at each model step. In terms of N, Q, and D_Q (three bulk properties), the simulated results of the BIN and BULK experiments show no significant differences in the upper cloud-containing model layers (−0.4 ~ −0.8 km) at the 30th minute (i.e., one model time step is done). However, the μ at the cloud top layers shows a substantial discrepancy between the BULK and BIN experiments. In terms of ice crystal fall distance, the difference between the BULK and BIN experiments is more obvious, owing to the reduction in dH to 100 m here. The N(bin) plot (lower panel) further shows the discrepancies in the ice crystal size distribution. As expected, the size distribution of ice crystals in the cloud top layer derived from the BULK experiment exhibits spurious concentration owing to the artificial adjustment imposed on μ, especially for the 30th minute. At the 120th minute, the BULK experiment simulation results show that there are nearly no small ice crystals (D< 10 μm) in the cloud-containing model layers. Actually, these small ice crystals remain mostly in the initial cloud-containing layers (i.e., the BIN experiment). This error of the BULK experiment is mainly induced by gamma fitting. The initial cloud thickness is 0.4 km for all ice crystal size bins. Theoretically, despite the longer falling distance of larger ice crystals, the cloud thickness for all size bins should remain at 0.4 km after 120 minutes. However, simulation results from the BIN experiment show that the cloud thickness for most size bins is greater than 0.4 km. This error is arising from the numerical diffusion. It is necessary to point out the 62nd bin, D(62)= 67.61 μm and V(62)= 5.55 cm s^{-1}. For this size bin, one model time step (i.e., 1800 s) leads to a fall distance of exactly one model layer (i.e., 100 m), with no subsequent numerical diffusion. This suggests that the simulation results with the bin scheme are also subject to computational errors (e.g., numerical diffusion). At last, the dT/dH ratio of these experiments (i.e., dH100dT1800) is 18 s m^{-1}, which is twice as that from dH200dT1800 experiments. Compared with the dH200dT1800 experiments, the differences between the BIN and BULK experiments are more pronounced here.

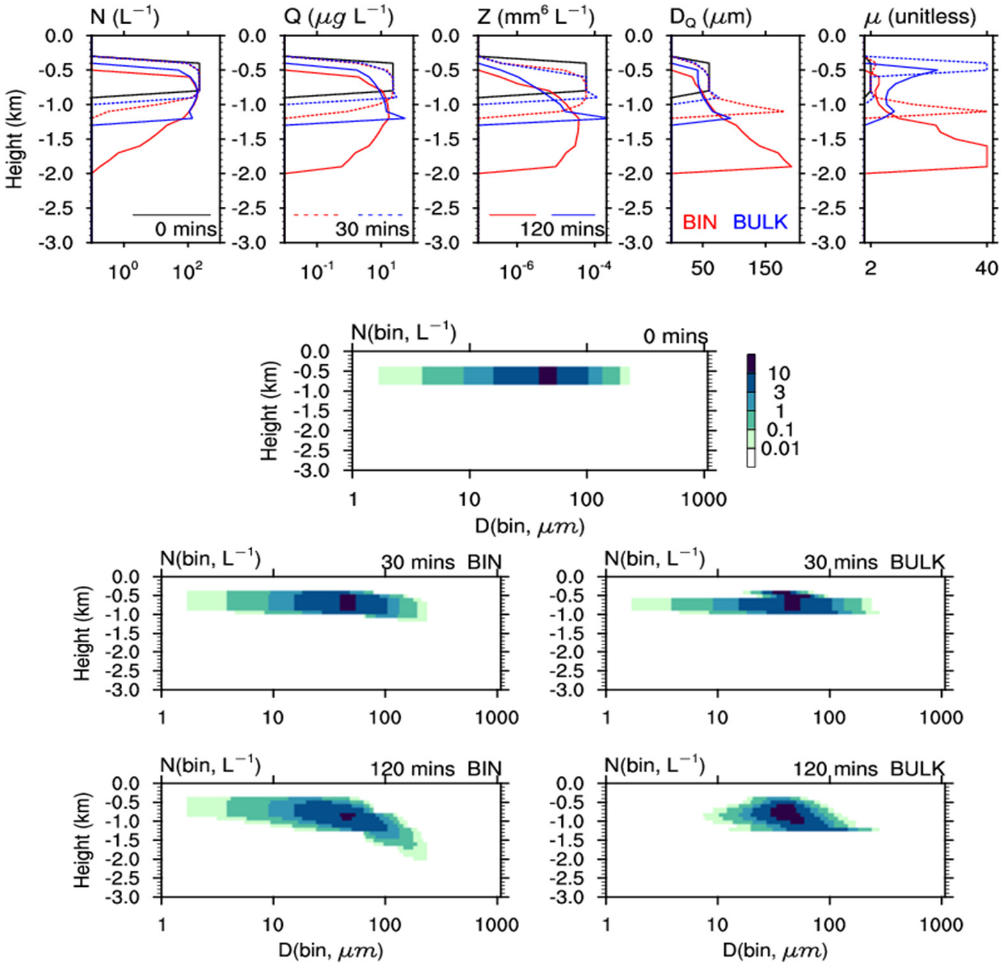

Figure 5. Similar as Figure 3, but for the dH100dT1800 experiments.

4. Discussion

In this study, the ice crystal sedimentation process is analyzed based on the initial size distribution scenario of D_Q= 60 μm and μ= 2. This scenario represents a common size distribution of ice crystals in cirrus clouds [48,91,120]. For smaller D_Q, the fall velocities are smaller, and numerical computational errors arising from the weighted fall velocity method (i.e., the bulk scheme) are reduced accordingly. Similarly, the bulk scheme yields much smaller sedimentation calculation errors for warm clouds, owing to the generally small size and slow fall velocity of cloud droplets. For larger μ, the discrepancies among the three weighted fall velocities (V_N, V_Q, and V_Z) are reduced as the size distribution becomes more concentrated. Consequently, the occurrence probability of inconsistencies in G(μ) is reduced. In other words, the sedimentation errors at cloud top are reduced.

Sedimentation process calculated by the bulk scheme may lead to spurious high values of μ at cloud top, which in turn alter the atmospheric radiation balance by altering the optical properties of cloud tops. Furthermore, the bulk scheme prevents large ice crystals from falling to second lower model layers, which may exert a certain influence on the evolution of cirrus clouds. While reducing the model time step can mitigate sedimentation errors, the setting of time steps in atmospheric models involves a compromise. It must account for other cloud microphysical processes (e.g., ice crystal collection) and other physical processes (e.g., cumulus convection). Given that climate models typically adopt a long time step (e.g., 1800 s) due to computational cost constraints, it may be worthwhile to try the following approach to mitigate sedimentation calculation errors. A hybrid bin-bulk scheme could be developed, using the bin scheme for sedimentation process calculations and the bulk scheme for other cloud microphysical processes.

5. Conclusions

This study investigates the sedimentation calculation errors arising from weighted fall velocities with the bulk schemes. These sedimentation calculation errors are illustrated via the comparisons of the simulation results from the bulk and bin schemes, even though the bin scheme also yields minor biases. To investigate the causes of these errors, this study presents a detailed account of how the bulk schemes calculate the sedimentation process. Since the weighted fall velocities (V_N, V_Q, and V_Z; $V_N < V_Q < V_Z$) present ice crystal instantaneous fluxes (N, Q, and Z) through a fixed altitude level, the bulk method inherently assumes that the falling ice crystals can only affect the adjacent model layer below. Furthermore, the weighted fall velocities might yield inconsistencies at certain spatiotemporal resolutions. These inconsistencies, coupled with the inherent assumption, are the main sources of error in sedimentation calculations.

Owing to the inherent assumption, the larger ice crystals can only fall into the adjacent layer below,which imposes a restriction on their falling distance. The impact of this restriction depends on the spatiotemporal resolution (i.e., dH and dT). Specifically, significant errors arise under conditions of smaller dH and larger dT. One inconsistency issue is as follows. Since V_Z is greater than V_Q and V_N, it may occur that the Z of ice crystals remaining in the current layer is extremely small after one model time step sedimentation, thereby yielding an extremely small G(μ) that falls outside the reasonable range. To address this, G(μ) is artificially constrained to the preset range, thereby introducing a spuriously high μ value. Whether this artificial adjustment is triggered depends on the spatiotemporal resolution, with higher frequency under conditions of smaller dH and larger dT. Another inconsistency also arises from the disparity in the three weighted fall velocities (i.e., V_N, V_Q, and V_Z), wherein a scenario with smaller dH and larger dT can lead to V_Z×dT exceeding dH while V_N×dT remains below it. In other words, the Z of ice crystals falls into the second lower layer, while the N of ice crystals falls into the adjacent (first) layer. While sub-stepping the time step alleviates this inconsistency, it does not remove the fundamental restriction that larger ice crystals can only reach the adjacent layer. In summary, the magnitude of sedimentation errors is dependent on the spatiotemporal resolution. For a standalone simulation of ice crystal sedimentation, these errors can be reduced to a negligible level by decreasing the dT/dH ratio.

 doi:10.20944/preprints202602.0956.v1

Author Contributions: X.S. designed this study and wrote the Fortran code of the 1D cloud model. X.S. and G.J. carried out the simulations used in this study and created all figures. X.S. wrote the manuscript. J.M. did some validation works. All authors have read and agreed to the published version of the manuscript.

Funding: This research was funded by the National Natural Science Foundation of China (grant nos. 42475174). The APC was supported by the same funder.

Institutional Review Board Statement: Not applicable.

Informed Consent Statement: Not applicable.

Data Availability Statement: The 1D cloud model source code (Fortran code and Makefile script), along with the simulation results used for plotting (comprising plotting scripts and raw images), have been archived in a public repository (https://doi.org/10.5281/zenodo.7589993, accessed on 7 February 2026).

Acknowledgments: This study was conducted at the High-Performance Computing Center of Nanjing University of Information Science and Technology. During the preparation of this manuscript, the authors used Doubao (online version, continuously updated) for the purposes of checking English writing grammar and moderately polishing the logical expression based on some revision suggestions. The authors have reviewed and edited the output and take full responsibility for the content of this publication.

Conflicts of Interest: The authors declare that they have no conflict of interest.

Abbreviations

Here is a list of symbols used in this manuscript:

Symbol	Description	Defaul value
$\Gamma(x)$	Gamma function, $\Gamma(x) = \int_0^\infty t^{x-1}e^{-t}\,\mathrm{d}t$	
N_0	Intercept parameter of gamma size distribution	
λ	Slope parameter of gamma size distribution	
μ	Shape parameter of gamma size distribution, $\mu \geq 0$	
D	Ice crystal diameter	
$N'(D)$	Number density of the ice crystals with diameter D, $N'(D) = N_0 D^{\mu} e^{-\lambda D}$	
M_k	the k$^{\text{th}}$ moment of gamma size distribution, $M_k = \int_0^\infty N_0 D^{\mu+k} e^{-\lambda D}\,\mathrm{d}D$	
ρ_i	Mass density of ice crystals	900 kg m^{-3}
c	A constant coefficient, $c = \rho_i \pi / 6$	
N	Ice crystal number per unit air volume, M_0	
Q	Ice crystal mass per unit air volume, cM_3	
Z	Ice crystal radar reflectivity factor per unit air volume, M_6	
D_Q	Mass-weighted ice crystal diameter, $D_Q = (Q/cN)^{1/3}$	
$G(\mu)$	A monotonic function of μ	
V	Ice crystal fall velocity	
V_N	Number-weighted ice crystal fall velocity	
V_Q	Mass-weighted ice crystal fall velocity	
V_Z	Radar reflectivity factor-weighted ice crystal fall velocity	
ρ_a	Air density, a function of temperature and pressure	
ρ_{a850}	Reference air density at 850 hPa and 273.15 K	
a	Fall velocity coefficient	700 m^{1-b} s^{-1}
b	Fall velocity coefficient	1

References

1. Liou, K.-N. Influence of cirrus clouds on weather and climate processes: A global perspective. *Mon. Wea. Rev.* **1986**, *114*, 1167–1199. https://doi.org/10.1175/1520-0493(1986)114<1167:IOCCOW>2.0.CO;2
2. Wang, P.-H.; Minnis, P.; McCormick, M.P.; Kent, G.S.; Skeens, K.M. A 6-year climatology of cloud occurrence frequency from Stratospheric Aerosol and Gas Experiment II observations (1985–1990). *J. Geophys. Res.* **1996**, *101*, 29407–29429. https://doi.org/10.1029/96JD01780
3. Khvorostyanov, V.I.; Sassen, K. Microphysical processes in cirrus and their impact on radiation: A mesoscale modeling perspective. In *Cirrus*; Lynch, D.K., Sassen, K., Starr, D.O.C., Stephens, G., Eds.; Oxford University Press: New York, NY, USA, 2002; pp. 397–432. https://doi.org/10.1093/oso/9780195130720.001
4. Luo, Z.; Rossow, W.B. Characterizing tropical cirrus life cycle, evolution, and interaction with upper-tropospheric water vapor using Lagrangian trajectory analysis of satellite observations. *J. Climate* **2004**, *17*, 4541–4563. https://doi.org/10.1175/3222.1
5. Gayet, J.F.; Shcherbakov, V.; Mannstein, H.; Minikin, A.; Schumann, U.; Ström, J.; Petzold, A.; Ovarlez, J.; Immler, F. Microphysical and optical properties of midlatitude cirrus clouds observed in the southern hemisphere during INCA. *Q. J. R. Meteorol. Soc.* **2006**, *132*, 2719–2748. https://doi.org/10.1256/qj.05.162
6. Li, J.; Mao, J. Simulation study of the effect of ice crystal properties on radiative characteristics of cirrus clouds. *Meteor. Mon.* **2006**, *32*, 9–13. 10.7519/j.issn.1000-0526.2006.2.002
7. Sassen, K.; Wang, Z.; Liu, D. Global distribution of cirrus clouds from CloudSat/Cloud-Aerosol Lidar and Infrared Pathfinder Satellite Observations (CALIPSO) measurements. *J. Geophys. Res.* **2008**, *113*, D00A12. https://doi.org/10.1029/2008JD009972
8. Mitchell, D.L.; Finnegan, W. Modification of cirrus clouds to reduce global warming. *Environ. Res. Lett.* **2009**, *4*, 045102. 10.1088/1748-9326/4/4/045102
9. Gao, Q.; Wang, G.; Shi, Y. Numerical study on a case of artificial precipitation enhancement of stratiform cloud system in North China. *Meteorol. Mon.* **2011**, *37*, 1241–1251.
10. Sheng, P.; Mao, J.; Li, J.; Ge, Z.; Zhang, A.; Sang, J.; Pan, N.; Zhang, H. *Atmospheric Physics*, 2nd ed.; Peking University Press: Beijing, China, 2013.
11. F Fu, Y.-F.; Qin, F. Summer daytime precipitation in ice, mixed, and water phase as viewed by PR and VIRS in tropics and subtropics. *Proc. SPIE* **2014**, *9259*, 925906. https://doi.org/10.1117/12.2069128
12. Li, R.; Cai, H.; Fu, Y.; Wang, Y.; Min, Q.; Guo, J.; Dong, X. The optical properties and longwave radiative forcing in the lateral boundary of cirrus cloud. *Geophys. Res. Lett.* **2014**, *41*, 3666–3675. https://doi.org/10.1002/2014GL059432
13. Zhu, S.; Guo, X. Aircraft measurements of ice crystal shape, distribution and growth process in stratiform-cumulus mixed clouds in North China. *Acta Meteorol. Sin.* **2014**, *72*, 366–389. 10.11676/qxxb2014.013
14. Bony, S.; Stevens, B.; Frierson, D.M.; Jakob, C.; Kageyama, M.; Pincus, R.; Shepherd, T.G.; Sherwood, S.C.; Siebesma, A.P.; Sobel, A.H. Clouds, circulation and climate sensitivity. *Nat. Geosci.* **2015**, *8*, 261–268. https://doi.org/10.1038/ngeo2398
15. Lu, Z.; Li, Y. Microphysical Properties of Deep Convection over the East China in Boreal Summer. *Meteorol. Disaster Reduct. Res.* **2016**, *39*, 81–89.
16. Zhou, C.; Zelinka, M.D.; Klein, S.A. Impact of decadal cloud variations on the Earth's energy budget. *Nat. Geosci.* **2016**, *9*, 871–874. https://doi.org/10.1038/ngeo2828
17. Deng, X.; Xue, H.; Meng, Z. The effect of ice nuclei on a deep convective cloud in South China. *Atmos. Res.* **2018**, *206*, 1–12. https://doi.org/10.1016/j.atmosres.2018.02.013
18. Ge, J.; Wang, Z.; Liu, Y.; Su, J.; Wang, C.; Dong, Z. Linkages between mid-latitude cirrus cloud properties and large-scale meteorology at the SACOL site. *Clim. Dyn.* **2019**, *53*, 5035–5046. https://doi.org/10.1007/s00382-019-04843-9
19. Hua, S.; Liu, Y.; Luo, R.; Shao, T.; Zhu, Q. Inconsistent aerosol indirect effects on water clouds and ice clouds over the Tibetan Plateau. *Int. J. Climatol.* **2020**, *40*, 3832–3848. https://doi.org/10.1002/joc.6430
20. Krämer, M.; Rolf, C.; Spelten, N.; Afchine, A.; Fahey, D.; Jensen, E.; Khaykin, S.; Kuhn, T.; Lawson, P.; Lykov, A. A microphysics guide to cirrus–Part 2: Climatologies of clouds and humidity from observations. *Atmos. Chem. Phys.* **2020**, *20*, 12569–12608. https://doi.org/10.5194/acp-20-12569-2020

 doi:10.20944/preprints202602.0956.v1

21. Zhao, F.; Tang, C.; Dai, C.; Wu, X.; Wei, H. The Global Distribution of Cirrus Clouds Reflectance Based on MODIS Level-3 Data. *Atmosphere* **2020**, *11*, 219. https://doi.org/10.3390/atmos11020219
22. Lloyd, G.; Gallagher, M.; Choularton, T.; Krämer, M.; Andreas, P.; Baumgardner, D. In Situ Measurements of Cirrus Clouds on a Global Scale. *Atmosphere* **2021**, *12*, 41. https://doi.org/10.3390/atmos12010041
23. Liu, J.; Shi, X. Estimating the potential cooling effect of cirrus thinning achieved via the seeding approach. *Atmos. Chem. Phys.* **2021**, *21*, 10609–10624. https://doi.org/10.5194/acp-21-10609-2021
24. Hou, T.; Chen, B.; Zhou, X.; Zhao, C.; Feng, Q.; Yan, F.; Zhou, W.; Cui, Y.; Du, Y.; Li, Z.; et al. Aircraft-based observations of ice concentrations in a midlatitude mixed-phase stratiform cloud system with embedded convection. *Atmos. Res.* **2023**, *281*, 106471. https://doi.org/10.1016/j.atmosres.2022.106471
25. Wang, Y.; Kong, R.; Cai, M.; Zhou, Y.; Song, C.; Liu, S.; Li, Q.; Chen, H.; Zhao, C. High small ice concentration in stratiform clouds over eastern China based on aircraft observations: Habit properties and potential roles of secondary ice production. *Atmos. Res.* **2023**, *281*, 106495. https://doi.org/10.1016/j.atmosres.2022.106495
26. Shi, X.; Liu, Y.; Liu, J. A Numerical Modeling Study on the Earth's Surface Brightening Effect of Cirrus Thinning. *Atmosphere* **2024**, *15*, 189. https://doi.org/10.3390/atmos15020189
27. Huang, G.; Su, Z.; Guan, L.; Zhang, J. Observation and analysis of the aggregation growth among ice-snow crystals. *J. Appl. Meteor. Sci.* **2007**, *18*, 561–567.
28. Krämer, M.; Schiller, C.; Afchine, A.; Bauer, R.; Gensch, I.; Mangold, A.; Schlicht, S.; Spelten, N.; Sitnikov, N.; Borrmann, S.; de Reus, M.; Spichtinger, P. Ice supersaturations and cirrus cloud crystal numbers. *Atmos. Chem. Phys.* **2009**, *9*, 3505–3522. https://doi.org/10.5194/acp-9-3505-2009
29. Murray, B.J.; Wilson, T.W.; Dobbie, S.; Cui, Z.; Al-Jumur, S.M.R.K.; Möhler, O.; Schnaiter, M.; Wagner, R.; Benz, S.; Niemand, M.; et al. Heterogeneous nucleation of ice particles on glassy aerosols under cirrus conditions. *Nat. Geosci.* **2010**, *3*, 233–237. https://doi.org/10.1038/ngeo817
30. Chen, B.; Zheng, K.; Guo, X. Numerical Investigation on the Growth of Large Hail in a Simulated Supercell Thunderstorm. *Climatic Environ. Res.* **2012**, *17*, 767–778. 10.3878/j.issn.1006-9585.2012.06.14
31. Cziczo, D.J.; Froyd, K.D.; Hoose, C.; Jensen, E.J.; Diao, M.; Zondlo, M.A.; Smith, J.B.; Twohy, C.H.; Murphy, D.M. Clarifying the dominant sources and mechanisms of cirrus cloud formation. *Sci.* **2013**, *340*, 1320–1324. https://doi.org/10.1126/science.1234145
32. Jensen, E.J.; Diskin, G.; Lawson, R.P.; Lance, S.; Bui, T.P.; Hlavka, D.; McGill, M.; Pfister, L.; Toon, O.B.; Gao, R. Ice nucleation and dehydration in the Tropical Tropopause Layer. *Proc. Natl. Acad. Sci. USA* **2013**, *110*, 2041–2046. https://doi.org/10.1073/pnas.1217104110
33. Jensen, E.; Lawson, R.; Bergman, J.; Pfister, L.; Bui, T.; Schmitt, C. Physical processes controlling ice concentrations in synoptically forced, midlatitude cirrus. *J. Geophys. Res. Atmos.* **2013**, *118*, 5348–5360. https://doi.org/10.1002/jgrd.50421
34. Li, X.; Zhou, Y.; Liu, L.; Wang, Y. A Case Test of Retrieving Stratus Microphysics Parameters from Millimeter-wave Cloud Radar. *J. Chengdu Univ. Inf. Technol.* **2013**, *28*, 274–283. 10.3969/j.issn.1671-1742.2013.03.012
35. Shi, X.; Liu, X.; Zhang, K. Effects of pre-existing ice crystals on cirrus clouds and comparison between different ice nucleation parameterizations with the Community Atmosphere Model (CAM5). *Atmos. Chem. Phys.* **2015**, *15*, 1503–1520. https://doi.org/10.5194/acp-15-1503-2015
36. Dinh, T.; Podglajen, A.; Hertzog, A.; Legras, B.; Plougonven, R. Effect of gravity wave temperature fluctuations on homogeneous ice nucleation in the tropical tropopause layer. *Atmos. Chem. Phys.* **2016**, *16*, 35–46. https://doi.org/10.5194/acp-16-35-2016
37. Qin, Q.; Zhang, L.; Yu, J.; Wu, L. Simulation study on phase state of two rain and snow processes in Beijing area. *Plateau Meteor.* **2019**, *38*, 1027–1037. 10.7522/j.issn.1000-0534.2018.00124
38. Shi, X.; Liu, X. Effect of cloud-scale vertical velocity on the contribution of homogeneous nucleation to cirrus formation and radiative forcing. *Geophys. Res. Lett.* **2016**, *43*, 6588–6595. https://doi.org/10.1002/2016GL069531
39. Li, Y.; Xiao, H.; Yang, H.; Sun, Y.; Zhou, Y.; Hu, Z.; Feng, X. Numerical Simulation of a Beijing Winter Snowstorm and its Cloud Microphysical Processes. *J. Chengdu Univ. Inf. Technol.* **2020**, *35*, 55–68. 10.16836/j.cnki.jcuit.2020.01.009

40. Li, X.; Su, J.; Wang, C.; Hu, X.; Wang, M.; Ge, J. Retrival of the terminal fall velocity of ice cloud particles and its spatiotemporal distribution characteristics at the SACOL. *Acta Meteorol. Sin.* **2020**, *78*, 1037–1049. 10.11676/qxxb2020.054
41. Zhou, W.; Lu, C.; Gao, W.; Deng, L. A modeling study of the evolution and microphysical mechanisms of a warm-sector heavy rainfall in South China. *J. Trop. Meteorol.* **2020**, *36*, 805–820. https://doi.org/10.16032/j.issn.1004-4965.2020.072
42. Zhang, Y.; Zheng, H.; Zhang, L.; Huang, Y.; Liu, X.; Wu, Z. Assessing the effect of riming on snow microphysics: The first observational study in East China. *J. Geophys. Res. Atmos.* **2021**, *126*, e2020JD034327. https://doi.org/10.1029/2020JD033763
43. Jensen, E.; Diskin, G.; DiGangi, J.; Woods, S.; Lawson, R.; Bui, T. Homogeneous Freezing Events Sampled in the Tropical Tropopause Layer. *J. Geophys. Res. Atmos.* **2022**, *127*, e2022JD036535. https://doi.org/10.1029/2022JD036535
44. Ren, S.; Gao, M.; Nan, Z.; Wang, M.; Li, Y. Effect of Polygonal Agglomerated Ice Crystals on Laser Scattering. *Atmosphere* **2022**, *13*, 369. https://doi.org/10.3390/atmos13030369
45. Kustova, N.; Konoshonkin, A.; Shishko, V.; Timofeev, D.; Tkachev, I.; Wang, Z.; Borovoi, A. Depolarization Ratio for Randomly Oriented Ice Crystals of Cirrus Clouds. *Atmosphere* **2022**, *13*, 1551. https://doi.org/10.3390/atmos13101551
46. Liu, Z.; Yin, Y.; Chen, Q.; Zou, Z.; Liang, X. The Response of Cloud Dynamic Structure and Microphysical Processes to Glaciogenic Seeding: A Numerical Study. *Atmosphere* **2025**, *16*, 1381. https://doi.org/10.3390/atmos16121381
47. Lin, W.; Meng, J.; Meng, W.; Fan, Q.; Li, J. Numerical simulation about a heavy snowfall event in North China: The sensitivity of cloud microphysical parameterization schemes. *Sci. Meteorol. Sin.* **2009**, *29*, 150–156.
48. Eidhammer, T.; Morrison, H.; Bansemer, A.; Gettelman, A.; Heymsfield, A.J. Comparison of ice cloud properties simulated by the Community Atmosphere Model (CAM5) with in-situ observations. *Atmos. Chem. Phys.* **2014**, *14*, 10103–10118. https://doi.org/10.5194/acp-14-10103-2014
49. Shen, X.; Mei, H.; Wang, W.; Huang, W. Numerical simulation of ice-phase processes using a double-moment microphysical scheme and a sensitivity test of ice nuclei concentration. *Chin. J. Atmos. Sci.* **2015**, *39*, 83–99. https://doi.org/10.3878/j.issn.1006-9895.1405.13310
50. Xin, J. Validation of an improved simulation scheme for ice crystal freezing growth process. In Proceedings of the 32nd Annual Meeting of the Chinese Meteorological Society, Tianjin, China, 14–16 October 2015; p. 396.
51. Erfani, E.; Mitchell, D.L. Developing and bounding ice particle mass- and area-dimension expressions for use in atmospheric models and remote sensing. *Atmos. Chem. Phys.* **2016**, *16*, 4379–4400. https://doi.org/10.5194/acp-16-4379-2016
52. Eidhammer, T.; Morrison, H.; Mitchell, D.; Gettelman, A.; Erfani, E. Improvements in global climate model microphysics using a consistent representation of ice particle properties. *J. Clim.* **2017**, *30*, 609–629. https://doi.org/10.1175/JCLI-D-16-0050.1
53. Xu, H.; Yin, J. Some key issues in developing the numerical model for artificial weather modification. *Acta Meteor. Sinica* **2017**, *75*, 57–66. https://doi.org/10.11676/qxxb2017.009
54. Kang, Y.; Jin, S.; Peng, X.; Yang, X.; Shang, K.; Wang, S. Comparative analysis of single-moment and double-moment microphysics schemes in WRF on the torrential rainfall event in North China during 19–21 July 2016. *Plateau Meteorol.* **2018**, *37*, 481–494.https://doi.org/10.7522/j.issn.1000-0534.2017.00026
55. Gu, X.; Li, G. Impact of cloud microphysical schemes on numerical simulation of a plateau shear line rainstorm event. *J. Yunnan Univ. (Nat. Sci. Ed.)* **2019**, *41*, 526–536. https://doi.org/10.7540/j.ynu.20180441
56. Kang, Z.; Zhou, Z.; Li, H. Analysis on the effects of different horizontal resolutions and microphysical schemes on the simulation of a rainstorm in central China. *Torrential Rain Disaster* **2019**, *38*, 658–667. 10.3969/j.issn.1004-9045.2019.06.011
57. Xu, H.; Li, X. Sensitivity of WRF model simulations to parametrizations of depositional growth of ice crystal during the landfall of Typhoon Fitow (2013). *Q. J. R. Meteorol. Soc.* **2019**, *145*, 2161–2180. https://doi.org/10.1002/qj.3549

58. Teng, F.; Li, D.; Jiang, D.; Yang, S.; Wang, H.; Lu, J.; Nie, A. Comparative analysis of simulations on a heavy snow event in Liaoning province using different cloud microphysical parameterization schemes. *Acta Meteorol. Sin.* **2020**, *78*, 608–622. 10.11676/qxxb2020.045
59. Yi, N.; Su, L.; Shi, J.; Dong, Z.; Xu, Z. Impact of Different Cloud Microphysics ParameterizationSchemes on Hail Simulation. *J. Arid Meteorol.* **2020**, *38*, 619–631.
60. Morrison, H.; van Lier-Walqui, M.; Fridlind, A.M.; Grabowski, W.W.; Harrington, J.Y.; Hoose, C.; Korolev, A.; Kumjian, M.R.; Milbrandt, J.A.; Pawlowska, H.; et al. Confronting the challenge of modeling cloud and precipitation microphysics. *J. Adv. Model. Earth Syst.* **2020**, *12*, e2019MS001689. https://doi.org/10.1029/2019MS001689
61. Hou, T.J.; Lei, H.C.; Hu, Z.X.; Yang, J.F.; Li, X.Y. Simulations of microphysics and precipitation in a stratiform cloud case over northern China: Comparison of two microphysics schemes. *Adv. Atmos. Sci.* **2020**, *37*, 117–129. https://doi.org/10.1007/s00376-019-8257-0
62. Ma, Z.; Liu, Q.; Sun, J.; Kong, Q.; Li, Z.; Shen, X.; Zhao, C.; Dai, K.; Tao, F. Study on the reason for overestimation of a snowfall case by WSM6 cloud microphysical scheme over North China. *Meteorol. Mon.* **2021**, *47*, 1029–1046. 10.7519/j.issn.1000-0526.2021.09.001
63. Zhou, Z.; Cui, C.; Hu, Y.; Kang, Z. Sensitivity of microphysical parameterization on the numerical simulation of a Meiyu front heavy rainfall process. *Chin. J. Atmos. Sci.* **2021**, *45*, 1292–1312. 10.3878/j.issn.1006-9895.2105.21025
64. Jiang, Z.; An, Y.; Yin, J. Comparison of Coupled Model Intercomparison Project Phases 5 and 6 in Simulating Diurnal Cloud Cycle. *Atmosphere* **2024**, *15*, 381. https://doi.org/10.3390/atmos15030381
65. Sankaré, H.; Blanchet, J.-P.; Laprise, R. Sensitivity of Atmospheric Energetics to Optically Thin Ice Clouds During the Arctic Polar Night. *Atmosphere* **2025**, *16*, 1329. https://doi.org/10.3390/atmos16121329
66. Wang, A.; Xie, X.; Dong, Z.; Li, X.; Shang, K.; Liu, X.; Xue, Z. Mitigating Model Biases in Arid Region Precipitation over Northwest China Through Dust–Cloud Microphysical Interactions. *Atmosphere* **2025**, *16*, 800. https://doi.org/10.3390/atmos16070800
67. Li, X.; Tao, W.K.; Khain, A.P.; Simpson, J.; Johnson, D.E. Sensitivity of a cloud-resolving model to bulk and explicit bin microphysical schemes. Part I: Comparisons. *J. Atmos. Sci.* **2009**, *66*, 3–21. https://doi.org/10.1175/2008JAS2646.1
68. Khain, A.P.; Beheng, K.D.; Heymsfield, A.; Korolev, A.; Krichak, S.O.; Levin, Z.; Pinsky, M.; Phillips, V.; Prabhakaran, T.; Teller, A.; et al. Representation of microphysical processes in cloud-resolving models: Spectral (bin) microphysics versus bulk parameterization. *Rev. Geophys.* **2015**, *53*, 247–322. 10.1002/2014RG000468
69. Hu, A.Z.; Igel, A.L. A bin and a bulk microphysics scheme can be more alike than two bin schemes. *J. Adv. Model. Earth Syst.* **2023**, *15*, e2022MS003303. https://doi.org/10.1029/2022MS003303
70. Liu, Y.G.; Yau, M.-K.; Shima, S.-I.; Lu, C.S.; Chen, S.S. Parameterization and explicit modeling of cloud microphysics: Approaches, challenges, and future directions. *Adv. Atmos. Sci.* **2023**, *40*, 747–790. https://doi.org/10.1007/s00376-022-2077-3
71. Ovtchinnikov, M.; Kogan, Y.L. An investigation of ice production mechanisms in small cumuliform clouds using a 3D model with explicit microphysics. Part I: Model description. *J. Atmos. Sci.* **2000**, *57*, 2989–3003. https://doi.org/10.1175/1520-0469(2000)057<2989:AIOIPM>2.0.CO;2
72. Khain, A.; Pokrovsky, A.; Pinsky, M.; Seifert, A.; Phillips, V. Simulation of effects of atmospheric aerosols on deep turbulent convective clouds using a spectral microphysics mixed-phase cumulus cloud model. Part I: Model description and possible applications. *J. Atmos. Sci.* **2004**, *61*, 2963–2982. https://doi.org/10.1175/JAS-3350.1
73. Iguchi, T.; Teruyuki, N.; Khain, A.; Saito, K.; Takemura, T.; Okamoto, H.; Nishizawa, T.; Tao, W. Evaluation of cloud microphysics simulated by a meso-scale model coupled with a bin-based scheme using observation data by W-band radar. In *AGU Fall Meeting Abstracts*; San Francisco, CA, USA, 14–18 December 2009; Abstract A21D-0272.
74. Khain, A.P.; Lynn, B.; Dudhia, J. Aerosol effects on intensity of landfalling hurricanes as seen from simulations with the WRF model with spectral bin microphysics. *J. Atmos. Sci.* **2010**, *67*, 365–384. https://doi.org/10.1175/2009JAS3210.1

75. Iguchi, T.; Nakajima, T.; Khain, A.P.; Saito, K.; Takemura, T.; Okamoto, H.; Nishizawa, T.; Tao, W. Evaluation of cloud microphysics in JMA-NHM simulations using bin or bulk microphysical schemes through comparison with cloud radar observations. *J. Atmos. Sci.* **2012**, *69*, 2566–2586. https://doi.org/10.1175/JAS-D-11-0213.1
76. Planche, C.; Wobrock, W.; Flossmann, A.I. The continuous melting process in a cloud-scale model using a bin microphysics scheme. *Q. J. R. Meteorol. Soc.* **2015**, *140*, 1986–1996. https://doi.org/10.1002/qj.2265
77. Morrison, H.; Curry, J.A.; Khvorostyanov, V.I. A new double-moment microphysics parameterization for application in cloud and climate models. Part I: Description. *J. Atmos. Sci.* **2005**, *62*, 1665–1677. https://doi.org/10.1175/jas3446.1
78. Seifert, A.; Beheng, K.D. A two-moment cloud microphysics parameterization for mixed-phase clouds. Part 1: Model description. *Meteorol. Atmos. Phys.* **2006**, *92*, 45–66. https://doi.org/10.1007/s00703-005-0112-4
79. Liu, X.; Penner, J.E.; Ghan, S.J.; Wang, M. Inclusion of ice microphysics in the NCAR community atmospheric model version 3 (CAM3). *J. Clim.* **2007**, *20*, 4526–4547. https://doi.org/10.1175/JCLI4264.1
80. Lohmann, U.; Stier, P.; Hoose, C.; Ferrachat, S.; Kloster, S.; Roeckner, E.; Zhang, J. Cloud microphysics and aerosol indirect effects in the global climate model ECHAM5-HAM. *Atmos. Chem. Phys.* **2007**, *7*, 3425–3446. https://doi.org/10.5194/acp-7-3425-2007
81. Kärcher, B.; Burkhardt, U. A cirrus cloud scheme for general circulation models. *Q. J. R. Meteorol. Soc.* **2008**, *134*, 1439–1461. https://doi.org/10.1002/qj.301
82. Spichtinger, P.; Gierens, K.M. Modelling of cirrus clouds–Part 1a: Model description and validation. *Atmos. Chem. Phys.* **2009**, *9*, 685–706. https://doi.org/10.5194/acp-9-685-2009
83. Salzmann, M.; Ming, Y.; Golaz, J.C.; Ginoux, P.A.; Morrison, H.; Gettelman, A.; Krämer, M.; Donner, L.J. Two-moment bulk stratiform cloud microphysics in the GFDL AM3 GCM: Description, evaluation, and sensitivity tests. *Atmos. Chem. Phys.* **2010**, *10*, 8037–8064. https://doi.org/10.5194/acp-10-8037-2010
84. Wang, M.; Penner, J.E. Cirrus clouds in a global climate model with a statistical cirrus cloud scheme. *Atmos. Chem. Phys.* **2010**, *10*, 5449–5474. https://doi.org/10.5194/acp-10-5449-2010
85. Shi, X.; Wang, B.; Liu, X.; Wang, M. Two-moment bulk stratiform cloud microphysics in the grid-point atmospheric model of IAP LASG (GAMIL). *Adv. Atmos. Sci.* **2013**, *30*, 868–883. https://doi.org/10.1007/s00376-012-2072-1
86. Gettelman, A.; Morrison, H. Advanced two-moment bulk microphysics for global models. Part I: Off-line tests and comparison with other schemes. *J. Clim.* **2015**, *28*, 1268–1287. https://doi.org/10.1175/JCLI-D-14-00102.1
87. Krämer, M.; Rolf, C.; Luebke, A.; Afchine, A.; Spelten, N.; Costa, A.; Meyer, J.; Zoeger, M.; Smith, J.; Herman, R.L. A microphysics guide to cirrus clouds–Part 1: Cirrus types. *Atmos. Chem. Phys.* **2016**, *16*, 3463–3483. https://doi.org/10.5194/acp-16-3463-2016
88. Zhang, G.; Wang, M.; Lu, C.; Bao, Q.; Wang, Y. Development and application of atmospheric physical process parameterization in high-resolution global climate models. *China Basic Sci.* **2017**, *19*, 40–44. 10.3969/j.issn.1009-2412.2017.05.008
89. Wang, L.; Bao, Q.; Wang, W.C.; Liu, Y.; Wu, G.X.; Zhou, L.; Li, J.; Gong, H.; Nian, G.; Li, J.; et al. LASG Global AGCM with a Two-moment Cloud Microphysics Scheme: Energy Balance and Cloud Radiative Forcing Characteristics. *Adv. Atmos. Sci.* **2019**, *36*, 697–710. https://doi.org/10.1007/s00376-019-8196-9
90. Li, J.; Peng, X.; Li, X.; Lin, Y.; Chu, W. Evaluation of a Flexible Single Ice Microphysics and a Gaussian Probability-Density-Function Macrophysics Scheme in a Single Column Model. *Atmosphere* **2021**, *12*, 638. https://doi.org/10.3390/atmos12050638
91. McFarquhar, G.M.; Hsieh, T.; Freer, M.; Mascio, J.; Jewett, B.F. The characterization of ice hydrometeor gamma size distributions as volumes in N_0–λ–μ phase space: Implications for microphysical process modeling. *J. Atmos. Sci.* **2015**, *72*, 892–909. https://doi.org/10.1175/JAS-D-14-0011
92. Morrison, H.; Milbrandt, J.A. Parameterization of cloud microphysics based on the prediction of bulk ice particle properties. Part I: Scheme description and idealized tests. *J. Atmos. Sci.* **2015**, *72*, 287–311. https://doi.org/10.1175/jas-d-14-0065.1

93. Khain, A.P.; Pinsky, M. Cloud Particles and Their Representation in Cloud Models. In *Physical Processes in Clouds and Cloud Modeling*; Cambridge University Press: Cambridge, UK, 2018; pp. 19–67. https://doi.org/10.1017/9781139049481.003
94. Morrison, H.; Gettelman, A. A new two-moment bulk stratiform cloud microphysics scheme in the community atmosphere model, version 3 (CAM3). Part I: Description and numerical tests. *J. Clim.* **2008**, *21*, 3642–3659. https://doi.org/10.1175/2008JCLI2105.1
95. Barahona, D.; Molod, A.; Bacmeister, J.; Nenes, A.; Gettelman, A.; Morrison, H.; Phillips, V.; Eichmann, A. Development of two-moment cloud microphysics for liquid and ice within the NASA Goddard Earth Observing System Model (GEOS-5). *Geosci. Model Dev.* **2014**, *7*, 1733–1766. https://doi.org/10.5194/gmd-7-1733-2014
96. Lin, Y.; Huang, X.; Liang, Y.; Qin, Y.; Xu, S.; Huang, W.; et al. Community Integrated Earth System Model (CIESM): Description and evaluation. *J. Adv. Model. Earth Syst.* **2020**, *12*, e2019MS002036. https://doi.org/10.1029/2019MS002036
97. Milbrandt, J.A.; Yau, M.K. A multimoment bulk microphysics parameterization. Part II: A proposed three-moment closure and scheme description. *J. Atmos. Sci.* **2005**, *62*, 3065–3081. https://doi.org/10.1175/jas3535.1
98. Loftus, A.M.; Cotton, W.R.; Carrió, G.G. A triple-moment hail bulk microphysics scheme. Part I: Description and initial evaluation. *Atmos. Res.* **2014**, *149*, 35–57. https://doi.org/10.1016/j.atmosres.2014.05.013
99. Paukert, M.; Fan, J.; Rasch, P.J.; Morrison, H.; Milbrandt, J.A.; Shpund, J.; Khain, A. Three-moment representation of rain in a bulk microphysics model. *J. Adv. Model. Earth Syst.* **2019**, *11*, 257–277. https://doi.org/10.1029/2018MS001512
100. Deng, W.; Sum, J.; Lei, H. Numerical Simulation Research on the Effects of the Size Distribution of Aerosols on the Droplet Spectrum with a Newly Developed Triple-Moment Bulk Scheme. *Clim. Environ. Res.* **2019**, *24*, 693–710. 10.3878/j.issn.1006-9585.2018.18048
101. Milbrandt, J.A.; Morrison, H.; Dawson II, D.T.; Paukert, M. A triple-moment representation of ice in the Predicted Particle Properties (P3) microphysics scheme. *J. Atmos. Sci.* **2021**, *78*, 439–458. https://doi.org/10.1175/jas-d-20-0084.1
102. Zhang, J.; Sun, J.; Deng, W.; Ma, Y. Newly Developed Multiparameter Bulk Cloud Schemes. Part I: A New Triple-Moment Condensation Scheme and Tests. *J. Atmos. Sci.* **2022**, *79*, 2645–2684. https://doi.org/10.1175/JAS-D-22-0039.1
103. Mallick, C.; Dutta, U.; Bhowmik, M.; et al. Comparison of Two-Moment and Three-Moment Bulk Microphysics Schemes in Thunderstorm Simulations over Indian Subcontinent. *Atmos. Res.* **2024**, *310*, 107614. https://doi.org/10.1016/j.atmosres.2024.107614
104. Müller, R.; Peter, T. The Numerical Modelling of the Sedimentation of Polar Stratospheric Cloud Particles. *Ber. Bunsenges. Phys. Chem.* **1992**, *96*, 353–361. https://doi.org/10.1002/bbpc.19920960323
105. Deng, M.; Mace, G.G. Cirrus cloud microphysical properties and air motion statistics using cloud radar Doppler moments: Water content, particle size, and sedimentation relationships. *Geophys. Res. Lett.* **2008**, *35*, 1648–1658. https://doi.org/10.1029/2008GL035054
106. Hong, S.Y.; Lim, K.-S.S.; Kim, J.H.; et al. Sensitivity Study of Cloud-Resolving Convective Simulations with WRF Using Two Bulk Microphysical Parameterizations: Ice-Phase Microphysics versus Sedimentation Effects. *J. Appl. Meteorol. Climatol.* **2009**, *48*, 61–76. https://doi.org/10.1175/2008JAMC1960.1
107. Zhang, Y.; Wang, D.; Yin, J.; Xu, H. Impacts of Terminal Velocity and Drop Size Distribution Shape on the Numerical Simulation of Precipitation. *Chin. J. Atmos. Sci.* **2016**, *40*, 841–852. 10.3878/j.issn.1006-9895.1504.15193
108. Donet, L.; Alfonso, L. Development and evaluation of a bulk three-moment parameterization scheme incorporating the processes of sedimentation and collision-coalescence. *Atmosfera* **2023**, *38*, 1–21. https://doi.org/10.20937/atm.53181
109. Milbrandt, J.A.; Yau, M.K. A multimoment bulk microphysics parameterization. Part I: Analysis of the role of the spectral shape parameter. *J. Atmos. Sci.* **2005**, *62*, 3051–3064. https://doi.org/10.1175/JAS3534.1

110. Loftus, A.M.; Cotton, W.R. A triple-moment hail bulk microphysics scheme. Part II: Verification and comparison with two-moment bulk microphysics. *Atmos. Res.* **2014**, *150*, 97–128. https://doi.org/10.1016/j.atmosres.2014.07.016
111. He, X.; Lu, C.; Shi, X.; Zhang, W.; Zhu, L.; Xu, X.; Li, J.; Li, D. Development of a triple-moment ice-phase cloud microphysics scheme and its application to the Single Column Atmosphere Model. *Chin. Sci. Bull.* **2022**, *15*, 1971–1984. https://doi.org/10.1360/TB-2022-0697
112. Zhang, W.; Shi, X.; Lu, C. Impacts of the ice-particle size distribution shape parameter on climate simulations with the Community Atmosphere Model Version 6 (CAM6). *Geosci. Model Dev.* **2022**, *15*, 7751–7766. https://doi.org/10.5194/gmd-15-7751-2022
113. Milbrandt, J.A.; McTaggart-Cowan, R. Sedimentation-induced errors in bulk microphysics schemes. *J. Atmos. Sci.* **2010**, *67*, 3931–3948. https://doi.org/10.1175/2010JAS3541.1
114. Falk, N.M.; Igel, A.L.; Igel, M.R. The Relative Impact of Ice Fall Speeds and Microphysics Parameterization Complexity on Supercell Evolution. *Mon. Wea. Rev.* **2019**, *147*, 2403–2415. https://doi.org/10.1175/MWR-D-18-0417.1
115. Kessler, E. *On the Distribution and Continuity of Water Substance in Atmospheric Circulations*; *Meteorol. Monogr.*, No. 32; Amer. Meteor. Soc.: Boston, MA, USA, 1969; pp. 84.
116. Heymsfield, A.J.; Bansemer, A.; Twohy, C.H. Refinements to ice particle mass dimensional and terminal velocity relationships for ice clouds. Part I: Temperature dependence. *J. Atmos. Sci.* **2007**, *64*, 1047–1067. https://doi.org/10.1175/JAS3890.1
117. Wacker, U.; Seifert, A. Evolution of rain water profiles resulting from pure sedimentation: Spectral vs. parameterized description. *Atmos. Res.* **2001**, *58*, 19–39. https://doi.org/10.1016/S0169-8095(01)00081-3
118. Richardson, L.F. *Weather Prediction by Numerical Process*, 2nd ed.; Cambridge University Press: Cambridge, UK, 2007; pp. 250.
119. Vreugdenhil, C.B.; Koren, B., Eds. *Numerical Methods for Advection-Diffusion Problems*; *Notes Numer. Fluid Mech.*, Vol. 45; Vieweg: Braunschweig/Wiesbaden, Germany, 1993.
120. Heymsfield, A.J. Properties of tropical and midlatitude ice cloud particle ensembles. Part II: Applications for mesoscale and climate models. *J. Atmos. Sci.* **2003**, *60*, 2592–2611. https://doi.org/10.1175/1520-0469(2003)060<2592:POTAMI>2.0.CO;2